Letter

Quench spectroscopy for Lieb-Liniger bosons in the presence of harmonic trap

Jiachen Yu [1,*] Yuanzhe Hu [1,*] Wenhan Chen [1] Jianing Yang [1] Xuzong Chen,[1,2,†] and Hepeng Yao [1,‡]
[1]School of Electronics, Peking University, Beijing 100871, China
[2]School of Computing and Artificial Intelligence, Fuyao University of Science and Technology, Fuzhou 350109, China

(Received 10 July 2025; accepted 23 November 2025; published 22 December 2025)

Quench spectroscopy has emerged as a powerful technique for probing the energy spectrum of various quantum phases for quantum systems from out-of-equilibrium dynamics. While its efficacy has been demonstrated in the homogeneous systems theoretically, most experimental setups feature a confining potential, such as a harmonic trap, which complicates the practical implementations. In this work, we experimentally probe the quench spectroscopy for one-dimensional bosons in optical lattices with the presence of a harmonic trap, and compare our results with the density matrix renormalization group simulation. For the Mott insulator phase, although a gap is still observed, the band signal is broadened along the frequency space and cut at the half Brillouin zone, which can be explained by the nearest-neighbor tunneling excitations under harmonic confinement. Comparing with the superfluid spectrum, we can see a clear distinction between the two phases and find that the inverse quench with larger amplitude yields the clearest spectrum. Our work offers pivotal insights into conducting quench spectroscopy effectively in practical systems.

DOI: 10.1103/f4jf-6gt5

Introduction. Spectroscopy methods are widely used to detect the excitation information of strongly correlated systems [1–6], which reveals physical properties like electronic conductivity, magnetic ordering, superconductivity, and superfluidity. The basic idea is to induce an excitation to the system and measure the corresponding response from which one can extract the demanded spectrum information and dynamical properties of the system. In physical experiments, spectroscopy methods are often realized by different pump-probe techniques, such as angle-resolved-photoemission spectroscopy (ARPES) [1,7] and neutron scattering [8].

Quantum phase transition in strongly correlated systems is a crucial topic in quantum simulation. Various detection techniques have been developed to distinct different quantum phases and probe their excitation properties. In cold-atom systems, time-of-flight imaging (TOF) is the most widely used one, which measures the momentum distributions and provides the information about quantum coherence. Judging from its interference pattern, one can distinguish the Mott insulator (MI) from the superfluid (SF) phase [9–13]. Other techniques such as the band mapping [14–17] or the quantum gas microscope [18–24] allow for further detecting the information about the band and the spatial distributions. On the spectroscopy side, Raman spectroscopy enables the probing of low-energy excitation spectra [25,26], while Bragg spectroscopy detects the dynamical structure factor and reveals systems' response spectra to density perturbations [27,28]. In addition, there are powerful approaches such as amplitude modulation spectroscopy, which measures excitation spectra [12,29], and measurements of critical velocity using moving optical lattices, which determines the onset of dissipation and superfluid breakdown [30].

In recent years, quench spectroscopy was proposed theoretically [31–33], which appears to be a powerful technique for detecting the excitation spectrum of various quantum phases, including the MI, SF, and even Bose glass phase in disordered systems [34–41]. Starting with a global quench, one subsequently measures the postquench evolution from which one can extract all elementary excitation information. In contrast to standard pump-probe techniques, it employs equal-time commutators to directly extract the dispersion relation of elementary excitations, which is experimentally more accessible. Moreover, it permits comprehensive spectral measurement in a single experimental run, eliminating the need for tedious momentum-space scanning. However, current research on quench spectroscopy remains largely theoretical and is only for the homogeneous case. In actual cold-atom experiments, there is usually a spatial confinement, mostly a harmonic trapping potential. The influence of such a confinement potential and the validation of quench spectroscopy methodology in such a situation remains unknown.

In this work, we carry out the quench spectroscopy experimentally for one-dimensional ultracold bosons in the presence of optical lattices and harmonic trap confinement. From the measured momentum distribution evolution after quench, we apply Fourier transform and obtain the quench spectral function (QSF) $S(k, \omega)$, which contains detailed information of

*These authors contributed equally to this work.
†Contact author: xuzongchen@pku.edu.cn
‡Contact author: hepeng.yao@pku.edu.cn

the energy spectrum. For the MI case, we quench to the same final MI phase from different initial lattice depths and find a modified signal of the Mott gap. More precisely, we detect a broadening of the bands' signal and a momentum cutoff at half of the first Brillouin zone, which can be explained by the additional excitations caused by the harmonic confinement. Nevertheless, we can still distinguish the QSF from the one of SF phase where no gap is detected. All these observed properties are in good agreement with the density matrix renormalization group (DMRG) simulations qualitatively. Furthermore, with statistical analysis, we estimate the gap visibility for our measurements and find the parameters with best visibility. Our work reveals the physical mechanism behind the modified QSF of confined 1D ultracold boson systems in an optical lattice and explores the optimal conditions for applying quench spectroscopy.

Model and approach. The dynamics of the system can be described by the time-dependent Schrödinger equation

$$i\hbar\frac{\partial}{\partial t}\psi(x,t)=\hat{H}\psi(x,t). \tag{1}$$

In this work, we consider a one-dimensional boson gas (Lieb-Liniger gas) in the presence of external potentials, whose Hamiltonian $\hat{H}$ is written as

$$\hat{H}=\sum_i\left(-\frac{\hbar^2}{2m}\frac{\partial^2}{\partial x_i^2}+V(x_i,t)\right)+g\sum_{i<j}\delta(x_i-x_j), \tag{2}$$

with m the mass of the particle, x_i the position of the ith particle, and g the 1D coupling constant decided by the 3D scattering length a_s and the transverse confinement potentials. The external potential consists of two parts. It writes

$$V(x,t)=V_x(t)\sin^2(kx)+\tfrac{1}{2}m\omega^2x^2, \tag{3}$$

where the first term is the periodic lattice potential along x direction with $k=\pi/a$ the wave vector of the lattice, a the lattice period, and $V_x(t)$ the lattice depth, which is quenched from $V_x(t=0)=V_x^i$ to $V_x(t>0)=V_x^f$ in the actual experiment. The second term is the harmonic potential V_{HT} induced by lattice beams along the transverse y–z directions with a trapping frequency ω.

Our experiment starts by preparing a nearly pure ^{87}Rb Bose-Einstein condensate (BEC) with atom number of about 8.0×10^4, scattering length $a_s=100.4a_0$, and temperature below 30 nK. Notably, the finite temperature only influences the relative intensity of the excitation spectrum and does not shift the energy positions of the spectral peaks (see more details in the Supplemental Material S4 [42]). Then we load the BEC into a three-dimensional optical lattice formed by three pairs of orthogonal retroreflected laser beams. As illustrated in Fig. 1(a), an array of one-dimensional tubes along x direction is generated by two strong lasers along y and z directions, forming 2D optical lattices with lattice depth $V_y=V_z=40E_{\mathrm{r}}$, with an uncertainty 5%–10%. The weighted average atom number in each tube is about $\bar{N}=45$. We further add one-dimensional optical lattice V_x (blue) along the tubes to carry out the quench spectroscopy. Due to the longitudinal distribution of the y–z lattice beams, a Gaussian profile is superposed to the x lattice, forming a harmonic trap in the center (black dashed line).

Figure 1(b) gives the phase diagram of the corresponding Bose-Hubbard model without the trap, $\hat{H}=-J\sum_i(\hat{a}_i^\dagger\hat{a}_{i+1}+\mathrm{H.c.})+\frac{U}{2}\sum_i\hat{n}_i(\hat{n}_i-1)-\mu\sum_i\hat{n}_i$, with J the tunneling between nearest neighbor, U the on-site interaction, and μ the chemical potential [26,31,43]. The Mott insulator lobe with filling $na=1$ appears in the strongly interacting regime, surrounded by superfluid phase. Due to the existence of the harmonic trap, the system can exhibit different phases at different sites. With the DMRG simulations (see details in the Supplemental Material S2 [42]), we find three typical density distributions [see inset of Fig. 1(b)]. At low enough potential, the system is an inhomogeneous superfluid, and we name it deep superfluid (D-SF) regime. Increasing the potential above $V_{c1}=9E_{\mathrm{r}}$, we find that the Mott plateaus appear and form the typical wedding cake shape with a superfluid region $na>1$ in the middle. Further increasing the potential above $V_{c2}=21E_{\mathrm{r}}$, the superfluid area with filling $na>1$ even disappears and the central part remains a large Mott plateau, which we name it deep Mott regime (D-MI). The three typical cases correspond to the three cuts (i)–(iii) in Fig. 1(b). According to this phase diagram, we select the final state of the quench to make sure the system is quenched into the D-MI or D-SF regime.

The time sequence of our experiment is shown in Fig. 1(c). We load the y–z lattices $V_y=V_z=40E_{\mathrm{r}}$ to form 1D tubes, which also causes the harmonic trap potential along the tubes V_{HT}. Correspondingly, the trap frequency of V_{HT} is $\omega=2\pi\times57.9$ Hz with an uncertainty below 5%. We also load the x lattice to the initial state of quench $V_x=V_x^i$ adiabatically in 80 ms, and then hold the system for 20 ms to reach equilibrium. At the moment $t=0$ ms, the lattice depth V_x is suddenly changed to the final state V_x^f, and then the system evolves for a time t_e. Finally, we shut down all the lattices and, after 30 ms ballistic expansion, we conduct the TOF detection; the imaging resolution of our system is 6.45 μm. In Fig. 1(d), we show one typical example of the data we obtain, for the case we quench from $V_x^i=18E_{\mathrm{r}}$ to $V_x^f=22E_{\mathrm{r}}$. For the evolution time t_e varying from 0 to 12 ms, we can get the momentum distribution $n(k_x,k_y,t)$ from TOF imaging along z direction. By integrating along y direction, we obtain the time evolution of the 1D momentum distribution $n(k_x,t)$. As suggested by Refs. [31,44,45], we can apply Fourier transform to the k or t variables, such that we can obtain the spreading of one-body correlation function $G^{(1)}(x,t)$ or the QSF $S(k,\omega)$, correspondingly. Noted that due to the breaking of translational invariance in the presence of V_{HT}, $G^{(1)}(x,t)$ here represents the integrated correlation function, which can be written as $G^{(1)}(x,t)=\int dx' g^{(1)}(x'+x,x')$ with $g^{(1)}(x'+x,x')=\langle\hat{\psi}^\dagger(x'+x,t)\hat{\psi}(x',t)\rangle$ the one-body correlation function for the homogeneous case. For details about data processing steps, see the Supplemental Material S3 [42].

Numerically, we simulate this model using the DMRG method [46,47] and time evolving block decimation algorithm based on TeNPy project [48]. For the initial state, we apply the particle-number operator at different positions to extract particle-number distribution $n(R)$. For each step of time evolution after quench, we apply the creation and annihilation operators at different positions and extract the one-body correlation function $G^{(1)}(x,t)$. Then, we can compute the momentum distribution $n(k,t)$ and the QSF $S(k,\omega)$

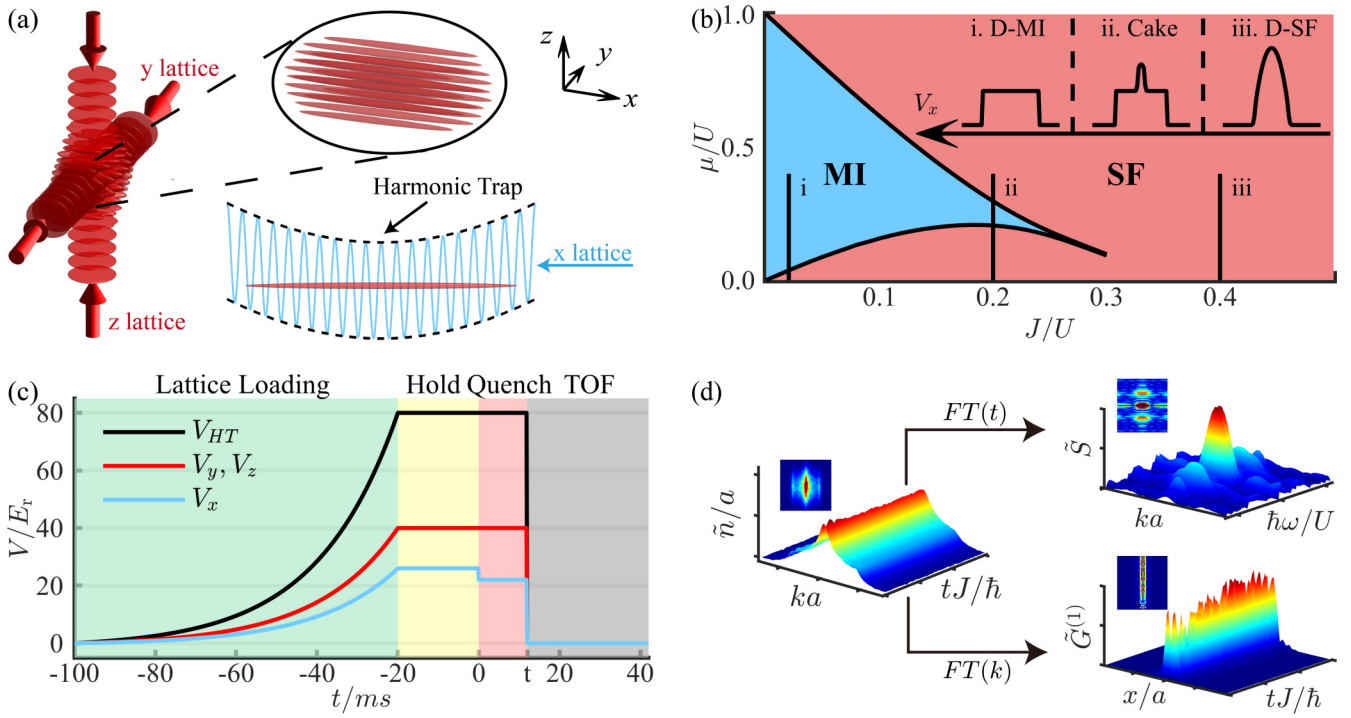

FIG. 1. The quench spectroscopy experiment. (a) Sketch of the experimental setup. With two strong lattice beams (y and z directions, red arrow), we form a bunch of one-dimensional atomic tubes (red arrays in set). Along the third direction, a relatively weak lattice (x direction, blue) is added, on top of the presenting harmonic trap (black dashed lines) induced by the y–z lattice beams. (b) Phase diagram for one-dimensional Bose-Hubbard model around the Mott lobe $na = 1$. SF (red) and MI (blue) phases are found at weak and strong interaction regimes, respectively. Graphs (i)–(iii) represent the three regimes we focused, as we changing the lattice depth along x direction V_x. The typical density distribution in real space is presented in the inset pictures. (c) The sequence of the quench spectroscope. Below $t = 0$ ms, we load the transverse lattices (y and z directions, red) and longitudinal lattices (x direction, blue) and hold the system for 20 ms. Correspondingly, a harmonic trap potential V_{HT} is induced (black). At $t = 0$ ms, we quench V_x. Then, all lasers are shut down at $t = 20$ ms and we perform the TOF detection. (d) Demonstration of data processing. From the TOF detection, we measure the momentum distribution evolution $n(k, t)$(left). By performing Fourier transform for parameter t or k, we obtain the QSF $S(k, \omega)$(right top) or correlation spreading $G^{(1)}(x, t)$, correspondingly. The insets show the top view.

by applying the Fourier transform. In the actual simulation, we use $L = 151a$ with open- boundary condition and various particle numbers averaged over different tubes in accordance with the experiment (see below and the Supplemental Material S5 [42]).

Quench spectroscopy for different phases. Firstly, we focus on the detection of the gap signal for the MI phase. With the presence of harmonic trap, it is not guaranteed that the information of the Mott gap still remains clearly in the QSF. Therefore, we first fix the final lattice depth $V_x^f = 22E_{\mathrm{r}}$ in the D-MI domain, and probe the QSF under different quench amplitudes. More precisely, we set the initial lattice depths V_x^i to $26E_{\mathrm{r}}$, $24.5E_{\mathrm{r}}$, and $23E_{\mathrm{r}}$, respectively. For each condition, the evolution time after quench t_e is gradually increased to 12 ms at a time interval of 0.2 ms. Under this condition, the maximum frequency we can detect is $\omega_{\max} \approx 2.42U/\hbar$ with a resolution $\Delta\omega \approx 0.08U/\hbar$, which is sufficient for our observations. Right after the quench stage, we obtain the momentum distribution evolution $n(k_x, t)$ by a 30 ms TOF detection. As illustrated in Fig. 1(d), we calculated the corresponding QSF and the results are shown in Fig. 2.

In Figs. 2(a)–2(c), we show the amplitude of measured QSF for different V_x^i to $V_x^f = 22E_{\mathrm{r}}$. The insets give the DMRG results for the corresponding experimental parameters. The DMRG simulation suggests that an energy gap $\Delta \sim U$ can be observed. However, instead of a sharp line as in the homogeneous case, this signal has a broadening of the linewidth $w_{\mathrm{DMRG}}(\hbar\omega = U) = 0.164U$. This can be understood by the nondegenerate nearest-neighbor tunneling excitations inside the Mott plateau with the presence of an inhomogeneous trap. In practice, it provides an energy shift of $\Delta V(i) = \pm(V_{\mathrm{HT}}(x_{i+1}) - V_{\mathrm{HT}}(x_i)) = \pm m\omega^2 a^2(2i + 1)/2$ for the excitation between the ith and $(i + 1)$th site, leading to a linewidth $w(\hbar\omega = U) = m\omega^2 a^2(2i_{\max} + 1)$. According to the DMRG simulation of the density profile, we have $i_{\max} = 21$, which is about half the width of the Mott plateau. It gives $w(\hbar\omega = U) = 0.170U$, which fits with our numerical simulation within 4%. In our experimental data, we also detect such a broadened signal around $\hbar\omega = U$, with width $w_{\mathrm{exp}}(\hbar\omega = U) = 0.212 \pm 0.023$. This fits with our theoretical prediction within 25%. Notably, the signals at $\hbar\omega = 0$ is also broadened into an ellipse shape, which is probably due to the tube distributions in actual experiment, and this is confirmed in our further DMRG calculation (see the Supplemental Material S5 [42]). Besides, the signal is strongest for an intermediate quench ($V_z = 24.5E_r \to 22E_r$), reflecting a balance between too small quenches, which produce only weak deviations from equilibrium, and too large ones, which overpopulate

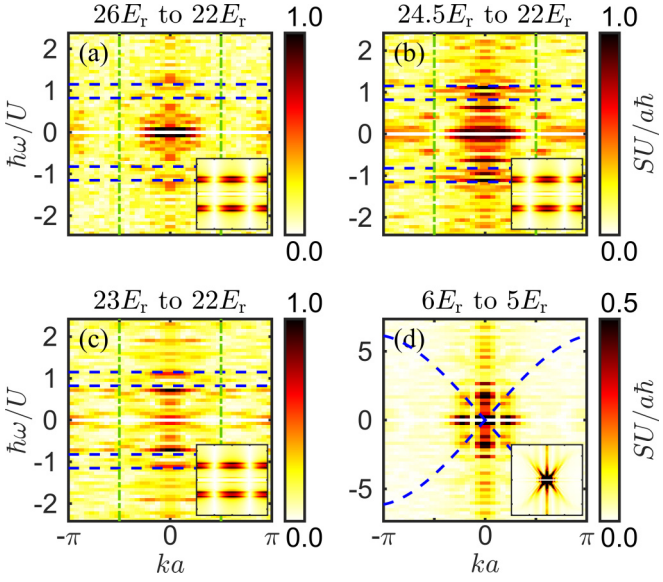

FIG. 2. QSF measured from the experiment when quenching from different initial trap depth V_x^i to a lower final depth V_x^f. (a). $V_x^i = 26E_r$ to $V_x^f = 22E_r$, (b) $V_x^i = 24.5E_r$ to $V_x^f = 22E_r$, (c) $V_x^i = 23E_r$ to $V_x^f = 22E_r$, (d) $V_x^i = 6E_r$ to $V_x^f = 5E_r$. Panels (a)–(c) are in the deep MI regime and panel (d) is in the deep SF regime. The values in each figure result from the average over six sets of experimental data, and the average relative error is around 20% (for details of error analysis, see the Supplemental Material S6 [42]). Inset figures represent the corresponding DMRG simulations. In panels (a)–(c), the blue and green dashed lines are guidance for the eyes to view the broadened peaks and momentum cutoff suggested by the simulation. The blue dashed curves in panel (d) are the Bogoliubov spectral branch suggested by the simulation result. The X axis represents k rescaled by $1/a$, Y axis is ω rescaled by $U/\hbar$. The colorbars represent $S(k, \omega)$ rescaled by $a\hbar/U$.

high-energy excitations and suppress the lowest branch. This observation provides useful insights for optimizing quench spectroscopy.

Moreover, both the experimental and the DMRG data show that the quench spectral function exhibits a clear suppression around $ka = \pi/2$, whereas a homogeneous system remains continuous in k. This effect can be attributed to the interference of two symmetric nearest-neighbor excitation, which is proportional to $\langle n|\hat{a}_k^\dagger \hat{a}_k|0\rangle\, \delta(E_n - \hbar\omega)$, with $|n\rangle$ excited state. In the Mott regime, the relevant excitations are nearest-neighbor doublon-holon pairs such as $\hat{a}^\dagger_{-(R+1)}\hat{a}_{-R}|g\rangle$ and $\hat{a}_{R+1}\hat{a}_R^\dagger|g\rangle$, which possess the same excitation energy and therefore interfere. Substituting these states yields a $\cos(ka)$ dependence of the matrix element, which vanishes at $k = \pi/2$ and accounts for the observed suppression. Furthermore, for $k > \pi/2$, high quasimomentum modes are particularly sensitive to phase coherence, so experimental decoherence further reduces the observable spectral weight.

Even though the harmonic trap tends to blur the information of the spectrum as discussed above, we can actually still distinguish the MI phase from the SF phase. To further prove this, we do the same experiment with the quench set from $V_x^i = 6E_r$ to $V_x^f = 5E_r$, see Fig. 2(d) with the inset showing the corresponding DMRG calculation. Under this condition, the system locates in the deep SF regime. In this picture, at $ka = 0$, we can clearly see a continuous distribution in both the experimental data and numerical simulations, which is the signature of gapless properties for the SF regime. By plotting a cut at $ka = 0$ and $ka = \pi/5$ for both of the four cases, we can clearly distinguish the gap and gapless signature between MI and SF phases, even with the presence of the harmonic trap. Notably, in the simulation data for the case in Fig. 2(d), we can also see a spectral branch extending from $S(0, 0)$ (see the blue dashed line, which is from the light yellow structure in inset), which agrees with the prediction based on Bogoliubov theory [49]. The strength of this spectral is only 2% of the maximum at k far from zero, which cannot be fully observed in actual experimental data due to the weakness of this signal.

Inverse quench and statistical analysis. To seek for better signal of the spectrum of the D-MI phase, we further test the inverse quench process, namely $V_x^i < V_x^f$. The final state is fixed at $V_x^f = 22E_r$, while the initial trap depths are set to $V_x^i = 20E_r$, $19E_r$, and $18E_r$ (see Fig. 3). We measure the QSF while keeping the other experimental parameters the same as in Figs. 2(a)–2(c). The first row in Fig. 3 is the results normalized to $S_{\max}U/a\hbar = 1$. At the zero momentum cut $ka = 0$, a clear gapped structure is observed for the case $V_x^i = 19E_r$ and $18E_r$. However, the high-momentum signal is weak. By setting the proper cutoff to the colorbars of each plot, we improve the visibility of the information inside [see Figs. 3(a2)–3(c2)]. The inset figures are the corresponding DMRG results.

From these data, we can conclude that with the decreasing of initial trap depth, the relative strength of the spectral branch also decrease, but the structure of spectral is even clearer, especially the high-momentum part. Moreover, comparing the quench with decreasing lattice depths, we find this inverse quench tends to give a better spectrum for our system. We attribute this to the fact that with a smaller initial potential, the corresponding equilibrium phase of V_x^i enters the cake regime, where more superfluid component enters into the density distributions with the presence of harmonic trap and the width of the Mott plateau also decreases (see the Supplemental Material S2 [42]). This causes additional gapless excitations around $\hbar\omega = 0$ due to superfluid-Mott tunneling, and clearer Mott gap excitation signals since the width of Mott plateau decreases. Notably, similarly as the cases in Figs. 2(a)–2(c), the band at $\hbar\omega = U$ has a width $w(\hbar\omega = U) = 0.203 \pm 0.015$, which fits the theoretical estimations within 20%. The main signal of these bands also ends around $k = \pi/2$ as predicted before.

We further evaluate the visibility of the energy gap in all the obtained QSF above. According to the previous discussions, the Mott insulator we detect has an energy gap U with a blurred width $w = 0.2U$. Thus, we define the gap visibility η as

$$\eta = \frac{\bar{I}_s}{\bar{I}_g} = \frac{\frac{1}{2w}\int_{U-w}^{U+w} S(k,\omega)d\omega}{\frac{1}{U-2w}\int_{w}^{U-w} S(k,\omega)d\omega}, \tag{4}$$

with $\bar{I}_s$ the average intensity within the area $[\pm U - w, \pm U + w]$ and $\bar{I}_g$ the average intensity of $[w, U - w]$. Figure 4(a) gives η at $ka = 0$ and $ka = \pi/5$ for all different experimental parameters in Figs. 2 and 3. The data at $V_x^i = 6E_r$ represent

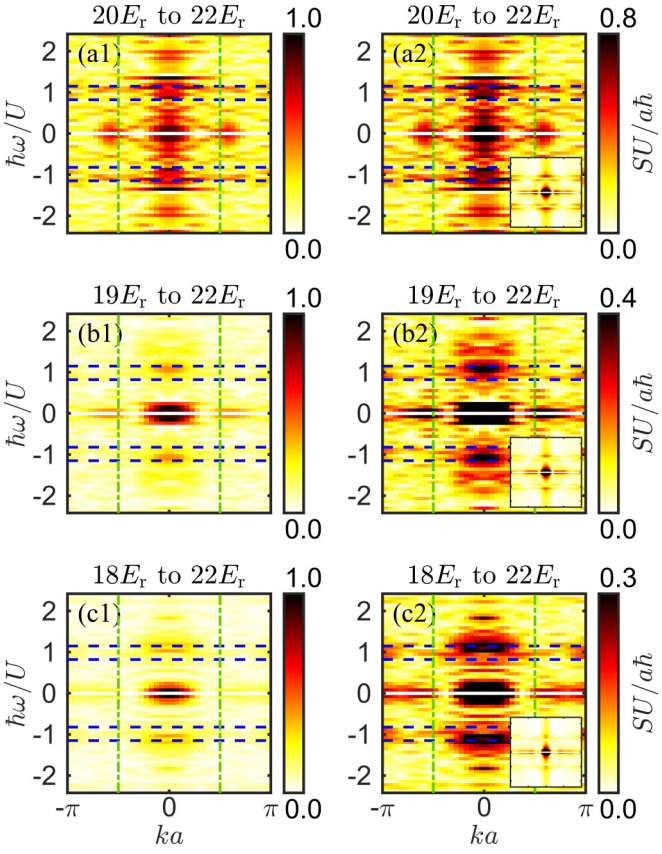

FIG. 3. Amplitude of QSF when quenching from different V_x^i to a higher $V_x^f = 22E_r$ in the deep MI phase. Panels (a)-(c) are cases quenching from different $V_x^i = 20E_r$, $19E_r$, and $18E_r$ to a fixed $V_x^f = 22E_r$, respectively. Panels (a1)–(c1) show the original QSF with the same range of colorbar, while panels (a2)–(c2) adjust the colorbar to reveal the detailed structure of the QSF. The values in each figure result from the average over six sets of experimental data and the average relative error is around 20%. Inset figures represent the corresponding DMRG simulations. The blue and green dashed lines are guidance for the eyes to view the broadened peaks and momentum cutoff suggested by the simulation. The axis and colorbars represent the same meaning as in Fig. 2.

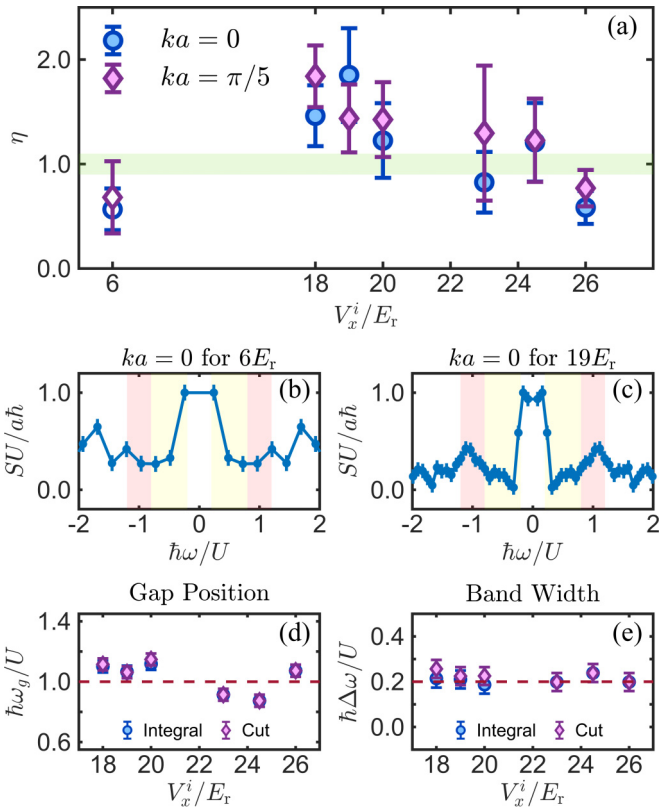

FIG. 4. Visibility of the energy gap. (a) η for different experiments. The blue and purple data points are calculated at cutting $ka = 0$ and $ka = \pi/5$, respectively. The light green area is the line $\eta = 1 \pm 0.1$ to guide the eyes. (b) Cutting at $ka = 0$ for SF quench. (c) Cutting at $ka = 0$ for MI quench from $19E_r$ to $22E_r$. The red and yellow regions in panels (b) and (c) represent the spectral area and gap area used to calculate η. (d) Position of the energy gap. The red dashed line shows the theory position $\hbar\omega/U = 1$. (e) Bandwidth of the energy gap. The red dashed line shows the position $\hbar\Delta\omega/U = 0.2$. The blue and purple data points in panels (d) and (e) are calculated according to integral and cut of $S(k, \omega)$, respectively.

SF quench from $6E_r$ to $5E_r$, and the others are MI quench from different V_x^i to $22E_r$. The light green area is the line $\eta = 1 \pm 0.1$ to guide the eyes. From the figure, we can see that for the SF case, $\eta(V_x^i = 6E_r)$ is clearly less than 1. While for the MI cases, η is larger than 1 for most of the cases. Especially, for the cases $V_x^i = 18E_r$ and $19E_r$, η is the largest and clearly more than the threshold $1 + 10\%$ we set. This fits with our previous statement that the case of the inverse quench with slightly larger quench amplitude shows the most obvious gap signals. Their QSF can be easily distinguished from the SF one.

Furthermore, we quantitatively evaluate the energy gap by estimating the position and width of the excited band. For the measured $S(k, \omega)$, we either take a cutoff at $ka = \pi/5$ or perform an integral between $ka = 0$ and $ka = \pi/2$, and evaluate the excited band position ω_g and width $\Delta\omega$, see Figs. 4(d) and 4(e) correspondingly (see more details in the Supplemental Material S6 [42]). From the integral method (blue circles), the average band position (equivalently gap width) is $\hbar\omega_g/U = 1.024 \pm 0.104$ and the average bandwidth is $\hbar\Delta\omega/U = 0.208 \pm 0.018$. From the cut method (purple diamonds), the average excited band position is $\hbar\omega_g/U = 1.031 \pm 0.111$ and the average bandwidth is $\hbar\Delta\omega/U = 0.224 \pm 0.022$. They both fit with our conclusion that a gap is observed at $\hbar\omega_g/U \simeq 1 \pm 0.1$.

Conclusion. In conclusion, we implement a quench spectroscopy for one-dimensional Bose-Hubbard model in the presence of harmonic trap. We observe a spectral branch at the position predicted theoretically. In contrast to homogeneous system, the spectral is a broadened area rather than a sharp line due to the existence of the harmonic trap. And the spectral has a cutoff at $ka = \pi/2$ at the same time. We attribute these phenomena to the nondegenerate nearest-neighbor excitations caused by the harmonic confinement. Moreover, we study the performance of the quench spectroscopy and compare spectral visibility of various quenches. We can see an obvious distinction between the two phases, and we find that we can

obtain a clearer spectrum when we perform an inverse quench with slightly larger quench amplitude.

Our research verifies the validity of quench spectroscopy for detecting the excitation spectrum of many-body quantum phases of 1D ultracold bosons in optical lattice with the presence of a potential confinement. In addition to simulate confined 1D Bose-Hubbard Model, it could also potentially be applied to the research of other models, such as Bose glass phase in disordered [44,45,50] or quasiperiodic systems [38,51], dipolar XY model [52], quantum spin chain [53,54], and dissipative non-Hermitian quantum lattice models [33].

Acknowledgments. We thank Laurent Sanchez-Palencia and Botao Wang for helpful discussions. This research was supported by the National Key Research and Development Program of China (Grants No. SQ2021YFA1400224, No. 2021YFA0718300, and No. 2021YFA1400900), the National Natural Science Foundation of China (Grant No. 11920101004), and the Fundamental Research Funds for the Central Universities, Peking University.

Data availability. The data that support the findings of this article are openly available [55].

[1] A. Damascelli, Probing the electronic structure of complex systems by ARPES, Phys. Scr. **2004**, 61 (2004).

[2] G. Roux, A. Minguzzi, and T. Roscilde, Dynamic structure factor of one-dimensional lattice bosons in a disordered potential: A spectral fingerprint of the Bose-glass phase, New J. Phys. **15**, 055003 (2013).

[3] T. Ernst, T. Paul, and P. Schlagheck, Transport of ultracold Bose gases beyond the Gross-Pitaevskii description, Phys. Rev. A **81**, 013631 (2010).

[4] V. Gritsev, E. Demler, M. Lukin, and A. Polkovnikov, Spectroscopy of collective excitations in interacting low-dimensional many-body systems using quench dynamics, Phys. Rev. Lett. **99**, 200404 (2007).

[5] S. Gupta, Z. Hadzibabic, M. W. Zwierlein, C. A. Stan, K. Dieckmann, C. H. Schunck, E. G. M. van Kempen, B. J. Verhaar, and W. Ketterle, Radio-frequency spectroscopy of ultracold fermions, Science **300**, 1723 (2003).

[6] H. Yao, L. Tanzi, L. Sanchez-Palencia, T. Giamarchi, G. Modugno, and C. D'Errico, Mott transition for a Lieb-Liniger gas in a shallow quasiperiodic potential: Delocalization induced by disorder, Phys. Rev. Lett. **133**, 123401 (2024).

[7] J. T. Stewart, J. P. Gaebler, and D. S. Jin, Using photoemission spectroscopy to probe a strongly interacting Fermi gas, Nature (London) **454**, 744 (2008).

[8] T.-H. Han, J. S. Helton, S. Chu, D. G. Nocera, J. A. Rodriguez-Rivera, C. Broholm, and Y. S. Lee, Fractionalized excitations in the spin-liquid state of a Kagome-lattice antiferromagnet, Nature (London) **492**, 406 (2012).

[9] E. Altman, E. Demler, and M. D. Lukin, Probing many-body states of ultracold atoms via noise correlations, Phys. Rev. A **70**, 013603 (2004).

[10] K. B. Davis, M. O. Mewes, M. R. Andrews, N. J. Van Druten, D. S. Durfee, D. M. Kurn, and W. Ketterle, Bose-Einstein condensation in a gas of sodium atoms, Phys. Rev. Lett. **75**, 3969 (1995).

[11] S. Richard, F. Gerbier, J. H. Thywissen, M. Hugbart, P. Bouyer, and A. Aspect, Momentum spectroscopy of 1D phase fluctuations in Bose-Einstein condensates, Phys. Rev. Lett. **91**, 010405 (2003).

[12] T. Stöferle, H. Moritz, C. Schori, M. Köhl, and T. Esslinger, Transition from a strongly interacting 1D superfluid to a Mott insulator, Phys. Rev. Lett. **92**, 130403 (2004).

[13] F. Gerbier, A. Widera, S. Fölling, O. Mandel, T. Gericke, and I. Bloch, Phase coherence of an atomic Mott insulator, Phys. Rev. Lett. **95**, 050404 (2005).

[14] M. Greiner, O. Mandel, T. Esslinger, T. W. Hänsch, and I. Bloch, Quantum phase transition from a superfluid to a Mott insulator in a gas of ultracold atoms, Nature (London) **415**, 39 (2002).

[15] I. B. Spielman, W. D. Phillips, and J. V. Porto, Mott-insulator transition in a two-dimensional atomic Bose gas, Phys. Rev. Lett. **98**, 080404 (2007).

[16] R. Jördens, N. Strohmaier, K. Günter, H. Moritz, and T. Esslinger, A Mott insulator of fermionic atoms in an optical lattice, Nature (London) **455**, 204 (2008).

[17] Q. Huang, Z. Zhu, Y. Wang, L. Liang, Q. Zheng, and X. Chen, Measurement of interacting quantum phases: A band mapping scheme, Front. Phys. **18**, 52307 (2023).

[18] M. Cheneau, P. Barmettler, D. Poletti, M. Endres, P. Schauß, T. Fukuhara, C. Gross, I. Bloch, C. Kollath, and S. Kuhr, Light-cone-like spreading of correlations in a quantum many-body system, Nature (London) **481**, 484 (2012).

[19] D. Greif, M. F. Parsons, A. Mazurenko, C. S. Chiu, S. Blatt, F. Huber, G. Ji, and M. Greiner, Site-resolved imaging of a fermionic Mott insulator, Science **351**, 953 (2016).

[20] K. D. Nelson, X. Li, and D. S. Weiss, Imaging single atoms in a three-dimensional array, Nat. Phys. **3**, 556 (2007).

[21] J. F. Sherson, C. Weitenberg, M. Endres, M. Cheneau, I. Bloch, and S. Kuhr, Single-atom-resolved fluorescence imaging of an atomic Mott insulator, Nature (London) **467**, 68 (2010).

[22] W. S. Bakr, J. I. Gillen, A. Peng, S. Fölling, and M. Greiner, A quantum gas microscope for detecting single atoms in a Hubbard-regime optical lattice, Nature (London) **462**, 74 (2009).

[23] C. Weitenberg, P. Schauß, T. Fukuhara, M. Cheneau, M. Endres, I. Bloch, and S. Kuhr, Coherent light scattering from a two-dimensional Mott insulator, Phys. Rev. Lett. **106**, 215301 (2011).

[24] E. Haller, J. Hudson, A. Kelly, D. A. Cotta, B. Peaudecerf, G. D. Bruce, and S. Kuhr, Single-atom imaging of fermions in a quantum-gas microscope, Nat. Phys. **11**, 738 (2015).

[25] T. P. Devereaux and R. Hackl, Inelastic light scattering from correlated electrons, Rev. Mod. Phys. **79**, 175 (2007).

[26] E. Haller, R. Hart, M. J. Mark, J. G. Danzl, L. Reichsöllner, M. Gustavsson, M. Dalmonte, G. Pupillo, and H.-C. Nägerl, Pinning quantum phase transition for a Luttinger liquid of strongly interacting bosons, Nature (London) **466**, 597 (2010).

[27] N. Fabbri, M. Panfil, D. Clément, L. Fallani, M. Inguscio, C. Fort, and J.-S. Caux, Dynamical structure factor of one-

dimensional Bose gases: Experimental signatures of beyond-Luttinger-liquid physics, Phys. Rev. A **91**, 043617 (2015).
[28] E. Altuntaş, R. G. Lena, S. Flannigan, A. J. Daley, and I. B. Spielman, Dynamical structure factor from weak measurements, Quantum Sci. Technol. **10**, 035045 (2025).
[29] M. Endres, T. Fukuhara, D. Pekker, M. Cheneau, P. Schauß, C. Gross, E. Demler, S. Kuhr, and I. Bloch, The 'Higgs' amplitude mode at the two-dimensional superfluid/Mott insulator transition, Nature (London) **487**, 454 (2012).
[30] J. Mun, P. Medley, G. K. Campbell, L. G. Marcassa, D. E. Pritchard, and W. Ketterle, Phase diagram for a Bose-Einstein condensate moving in an optical lattice, Phys. Rev. Lett. **99**, 150604 (2007).
[31] L. Villa, J. Despres, and L. Sanchez-Palencia, Unraveling the excitation spectrum of many-body systems from quantum quenches, Phys. Rev. A **100**, 063632 (2019).
[32] L. Villa, J. Despres, S. J. Thomson, and L. Sanchez-Palencia, Local quench spectroscopy of many-body quantum systems, Phys. Rev. A **102**, 033337 (2020).
[33] J. Despres, Quench spectroscopy for dissipative and non-Hermitian quantum lattice models, Phys. Rev. A **112**, 033320 (2025).
[34] T. Giamarchi and H. J. Schulz, Localization and interactions in one-dimensional quantum fluids, Europhys. Lett. **3**, 1287 (1987).
[35] T. Giamarchi and H. J. Schulz, Anderson localization and interactions in one-dimensional metals, Phys. Rev. B **37**, 325 (1988).
[36] C. D'Errico, E. Lucioni, L. Tanzi, L. Gori, G. Roux, I. P. McCulloch, T. Giamarchi, M. Inguscio, and G. Modugno, Observation of a disordered bosonic insulator from weak to strong interactions, Phys. Rev. Lett. **113**, 095301 (2014).
[37] Z. Zhu, H. Yao, and L. Sanchez-Palencia, Thermodynamic phase diagram of two-dimensional bosons in a quasicrystal potential, Phys. Rev. Lett. **130**, 220402 (2023).
[38] H. Yao, T. Giamarchi, and L. Sanchez-Palencia, Lieb-Liniger bosons in a shallow quasiperiodic potential: Bose glass phase and fractal Mott lobes, Phys. Rev. Lett. **125**, 060401 (2020).
[39] M. Yan, H.-Y. Hui, M. Rigol, and V. W. Scarola, Equilibration dynamics of strongly interacting bosons in 2D lattices with disorder, Phys. Rev. Lett. **119**, 073002 (2017).
[40] M. Yan, H.-Y. Hui, and V. W. Scarola, Dynamics of disordered states in the Bose-Hubbard model with confinement, Phys. Rev. A **95**, 053624 (2017).
[41] P. Russ, M. Yan, N. Kowalski, L. Wadleigh, V. W. Scarola, and B. DeMarco, Compressibility measurement of the thermal MI–BG transition in an optical lattice, arXiv:2506.16466.
[42] See Supplemental Material at https://link.aps.org/supplemental/10.1103/f4jf-6gt5 for details about DMRG method, density distribution in harmonic trap, data processing steps, finite temperature effect, atom number distribution effect, and analysis of experimental data, which includes Refs. [56–59].
[43] G. Boéris, L. Gori, M. D. Hoogerland, A. Kumar, E. Lucioni, L. Tanzi, M. Inguscio, T. Giamarchi, C. D'Errico, G. Carleo, G. Modugno, and L. Sanchez-Palencia, Mott transition for strongly interacting one-dimensional bosons in a shallow periodic potential, Phys. Rev. A **93**, 011601(R) (2016).
[44] L. Villa, S. J. Thomson, and L. Sanchez-Palencia, Quench spectroscopy of a disordered quantum system, Phys. Rev. A **104**, L021301 (2021).
[45] L. Villa, S. J. Thomson, and L. Sanchez-Palencia, Finding the phase diagram of strongly correlated disordered bosons using quantum quenches, Phys. Rev. A **104**, 023323 (2021).
[46] S. R. White, Density matrix formulation for quantum renormalization groups, Phys. Rev. Lett. **69**, 2863 (1992).
[47] U. Schollwöck, The density-matrix renormalization group in the age of matrix product states, Ann. Phys. (NY) **326**, 96 (2011).
[48] J. Hauschild, *et al.*, Tensor network Python (TeNPy) version 1, SciPost Phys. Codebases 41 (2024).
[49] L. P. Pitaevskii and S. Stringari, *Bose-Einstein Condensation* (Clarendon Press, Oxford, 2004).
[50] J. Smith, A. Lee, P. Richerme, B. Neyenhuis, P. W. Hess, P. Hauke, M. Heyl, D. A. Huse, and C. Monroe, Many-body localization in a quantum simulator with programmable random disorder, Nat. Phys. **12**, 907 (2016).
[51] R. Gautier, H. Yao, and L. Sanchez-Palencia, Strongly interacting bosons in a two-dimensional quasicrystal lattice, Phys. Rev. Lett. **126**, 110401 (2021).
[52] C. Chen, G. Emperauger, G. Bornet, F. Caleca, B. Gély, M. Bintz, S. Chatterjee, V. Liu, D. Barredo, N. Y. Yao, T. Lahaye, F. Mezzacapo, T. Roscilde, and A. Browaeys, Spectroscopy of elementary excitations from quench dynamics in a dipolar XY Rydberg simulator, Science **389**, 483 (2025).
[53] S. Bocini, F. Caleca, F. Mezzacapo, and T. Roscilde, Nonlocal quench spectroscopy of fermionic excitations in quantum spin chains, Phys. Rev. B **111**, L121114 (2025).
[54] J. T. Schneider, J. Despres, S. J. Thomson, L. Tagliacozzo, and L. Sanchez-Palencia, Spreading of correlations and entanglement in the long-range transverse Ising chain, Phys. Rev. Res. **3**, L012022 (2021).
[55] J. Yu, Y. Hu, W. Chen, J. Yang, X. Chen, and H. Yao, Quench spectroscopy for Lieb-Liniger bosons in the presence of harmonic trap, Zenodo (2025), https://zenodo.org/records/16791072.
[56] I. Bloch, J. Dalibard, and W. Zwerger, Many-body physics with ultracold gases, Rev. Mod. Phys. **80**, 885 (2008).
[57] B. Goyal, A. Dogra, S. Agrawal, B. Sohi, and A. Sharma, Image denoising review: From classical to state-of-the-art approaches, Inf. Fusion **55**, 220 (2020).
[58] M. Wang, S. Zheng, X. Li, and X. Qin, A new image denoising method based on Gaussian filter, in *2014 International Conference on Information Science, Electronics and Electrical Engineering* (IEEE, Sapporo, Japan, 2014), Vol. 1, pp. 163–167.
[59] Q. Huang, H. Yao, X. Chen, and L. Sanchez-Palencia, Direct measurement of tan's contact in a one-dimensional Lieb-Liniger gas, Sci. Adv. **11**, eadv3727 (2025).